Variability in the Upper-Ocean Internal Wave Field at a Sargasso Sea Site

CHARLES C. ERIKSEN

School of Oceanography, University of Washington, Seattle, Washington

(Manuscript received 2 June 1987, in final form 4 April 1988)

ABSTRACT

Two 3.5 month time series records of upper-ocean current and density profiles collected in opposite seasons as part of the LOTUS (Long-Term Upper-Ocean Study) project at 34°N, 70°W indicate substantial variation in the shape of horizontal current spectra in the internal wave frequency range. The near-inertial peak in these records shifts by as much as 10% in frequency and varies by a factor of 5 in height across the depth range of the seasonal pycnocline. Near-inertial currents are weaker and less strongly circularly polarized in the spring–summer than in the fall–winter record. Spectral frequency and vertical wavenumber dependences differ from those predicted by the Garrett–Munk internal wave model. Energy fluxes are vertically asymmetric and internal wave energy varies linearly with rms subinertial current speed.

Several aspects of the observed variability can be understood through two simple models. Depth dependence of near-inertial motions can be explained as a characteristic of linear response to forcing by random moving wind systems. Temporal variations in the shape, level, and polarization of current spectra can be explained as modulation of the deep-ocean internal wave spectrum through conservation of wave action flux as low-frequency, large vertical scale, weakly horizontally sheared currents are encountered.

1. Introduction

The oceanic internal wave field has been recognized for some time to be more variable within and above the seasonal thermocline than in the deep ocean (see Levine 1983). An obvious source of variability in the upper ocean is atmospheric variability, yet attempts to make a connection between wind forcing and internal wave response have been somewhat frustrating. Although bursts of internal wave energy are observed in the open ocean, at moderate frequencies within the internal wave band as well as near the inertial frequency, there is no clear correspondence with events in the local wind measured at the same open ocean site (Briscoe and Weller 1984). This lack of correspondence can be attributed both to an incomplete knowledge of the forcing field and to variation of the medium through which internal waves propagate.

Measurements of current, temperature, and salinity and several meteorological variables were made from ships and moorings over a two-year period at an open ocean site in the Sargasso Sea, 34°N, 70°W, in a project named LOTUS (Long-Term Upper-Ocean Study). Two of the main scientific goals of the experiment were to "obtain a description of the local response of the upper ocean to a potpourri of atmospheric forcing in a variety of environmental situations, such as in the presence of Gulf Stream rings or near oceanic fronts, and even to try to describe the statistical response to the fluctuating forcing" (Briscoe and Weller 1984). As part of the project, an upper-ocean moored current and density profiler developed by the C. S. Draper Laboratory, called the Profiling Current Meter (or PCM) obtained two 3.5-month records in opposite seasons, spring–summer and fall–winter. These records describe both a variety of environmental situations and considerable variability in the internal wave field.

The thesis of this work is that upper ocean internal wave variability at LOTUS can be understood as the combined result of both response to local atmospheric forcing and modulation by mesoscale current fluctuations of internal waves forced elsewhere, including the deep ocean. Although no correspondence between local meteorology and internal wave spectral levels is found, the near-inertial portion of frequency spectra of upper-ocean current vary in depth in a manner which can be explained as the response to random translating wind stress patterns. Across the band of internal wave frequencies resolvable in the PCM records (periods from inertial to 8 h), temporal variations in the spectrum of currents can be explained by interaction of the quasi-universal deep ocean internal wave field with mesoscale currents.

This paper is organized to demonstrate these two aspects of internal wave variability in turn after descriptions of the data acquisition and handling (section 2), the low frequency environment (section 3), depth variation of frequency spectra (section 4), and temporal variation of internal wave variance and its relationship to external variables (section 5). Section 6

Corresponding author address: Dr. Charles C. Eriksen, School of Oceanography, WB-10, University of Washington, Seattle, WA 98195.

presents an adaptation to LOTUS-region stratification of a model of Kundu and Thomson (1985) for oceanic response to a moving atmospheric front. This model explains the observed feature of inertial peak height depth variation and blue shift (to higher frequencies) with depth. Section 7 presents a model for modulating a spectrum of internal waves by parallel horizontally sheared barotropic mean flow. This model idealizes the interaction of internal waves with mesoscale eddy variability to the familiar ray theory concept of conservation of wave action flux normal to a mean flow. This model both accounts for slow temporal changes in frequency spectra and predicts features of the observed joint frequency–vertical wavenumber spectra presented in section 8. A discussion and summary appears in the last section.

Quantitative fits of model predictions to observed internal wave variability are not made in this work because the detailed environmental information necessary to attempt them was not collected. For the two models considered, detailed spatial and temporal descriptions of the wind stress and current fields needed to have been obtained to test the hypotheses in a statistically credible way. Short of having these descriptions, the models may be tested to see if they give plausible results given typical environmental inputs. Both models presented here predict observable features that are relatively insensitive to the details of these inputs. These features are quantitatively similar to what was observed during LOTUS.

2. Observational program and data handling

The data discussed here come from two PCM deployments in LOTUS. These were made with the unit S/N 01, a unit which served as an engineering prototype for later instruments. It collected 662 profiles starting 16 April 1983, at 34°00′N, 69°56′W in a record referred to here as P1G. After recovery on 3 August 1983, it was set again on 3 November 1983 at 34°00′N, 70°02′W and collected 629 profiles before depleting its battery power source in a record referred to here as P1H. (G and H refer to the seventh and eighth deployments of PCM S/N 01.) The interval between profiles was 4 hours, and the planned depth interval for each profile was 30–180 m for both deployments. The instrument typically required about 25 min to ascend through this depth range, during which it averaged measurements of east and north current, temperature, and electrical conductivity made at 1 Hz into preselected contiguous depth bins of 5 m thickness. Averaging into depth bins was equivalent to averaging in time over roughly 50 s duration, comparable to several periods of typical energetic surface gravity waves. Details of PCM design and performance are given by Eriksen et al. (1982).

The mooring for each deployment was a near-surface all wire rope design consisting of an upper section along which the PCM is free to move by buoyancy adjustment and a deeper section of a conventional distributed-buoyancy design. The mooring reacts to drag forces distributed along it by depressing during events of strong current of large vertical scale, limiting the shallowest depth the PCM can reach during its profiles. In order to conserve battery energy and to prevent it from nearing its crush depth, it is programmed to attempt a profile whenever it falls deeper than a given depth, chosen for these deployments to be 210 m. Buoyancy control at greater depths increases PCM electrical power consumption, thus shortening records.

The moorings were set and recovered from R/V *Oceanus* or R/V *Endeavor* on LOTUS cruises. After setting the mooring, at least one shallow conductivity–temperature–depth (CTD) cast was made in the vicinity of the mooring in order to calibrate the inductive electrical conductivity cell carried on the PCM. During the P1H deployment a CTD cast was made nearly 3 months after the PCM was set. The salinity calibration made from this cast agreed to within 0.01 practical salinity units (psu) of that made at the time of deployment, indicating that calibration drift is small relative to environmental variability.

In processing PCM data, profiles were edited for obvious noisy points, electrical conductivity was converted to salinity, the profiles were smoothed vertically with a triangular filter of 10 m half-width, and they were interpolated to an even grid in time using piecewise cubic splines. The records were divided into 9-day by 100 m (54 profile by 20 bin) data pieces for spectral analysis. The start times of these pieces are given in Table 1. The pieces were chosen to cover a uniform depth range (80–180 m) and be the minimum duration to resolve diurnal from inertial frequencies. (The 9th and 10th Fourier coefficients resolvable in these 9-day pieces are centered at frequencies 1 cycle per 24.00 h and 1 cycle per 21.60 h, respectively, where the inertial period at the LOTUS site is 21.46 h.)

In addition to analyzing the data on a depth–time grid, horizontal current records were scaled and mapped to a stretched depth–time grid according to WKBJ scaling of the vertical structure equation for nearly hydrostatic motions of a stratified fluid. To obtain the scaling and stretching factors, profiles of buoyancy frequency squared $N^2(z)$ were calculated and averaged together over each 9-day data piece. These average values were used to form scaled current records ($\mathbf{u}'$) from the measured values $\mathbf{u}$ according to the relation

$$\mathbf{u}(z') = [N_0/N(z)]^{1/2}\mathbf{u}(z)$$

where $N_0 = 1$ cph is a reference buoyancy frequency and the stretched upward coordinate z' is related to z by $dz = [N_0/N(z)]dz'$. The scaled currents $\mathbf{u}'(z')$ were then interpolated to a uniform grid in the stretched coordinate z' for use in spectral analysis. This scaling and stretching procedure was intended to account for

TABLE 1. Data pieces used in computing spectral quantities from PCM profiles. Each data piece consists of 54 successive profiles (9 day piece-lengths) over 20 depth bins (depth range 80–180 m).

Piece number	Start time (UTC)	Date	Year day
		P1G	
1	0200	17 Apr 1983	107
2	0200	26 Apr	116
3	2200	12 May	132
4	2200	21 May	141
5	2200	7 Jun	158
6	2200	16 Jun	167
7	2200	25 Jun	176
8	2200	4 Jul	185
9	2200	13 Jul	194
10	2200	22 Jul	203
		P1H	
1	1000	3 Nov	307
2	1000	12 Nov	316
3	1000	21 Nov	325
4	1000	30 Nov	334
5	1000	9 Dec	343
6	1000	18 Dec	352
7	1000	27 Dec	361
8	1000	5 Jan 1984	5
9	1000	14 Jan	14
10	1000	23 Jan	23

changes in amplitude and scale induced by stratification changes both in depth (through the seasonal pycnocline) and over time (on scales much longer than internal wave periods but short enough to resolve seasonal changes).

Standard techniques of time series analysis were applied to the depth–time and stretched depth–time gridded records. Instead of expressing horizontal current in Cartesian (east and north) components, they were transformed into rotary components (rotating clockwise and anticlockwise with increasing time). Autospectra of these components at each depth bin were calculated from each record (averaging over ten 9-day data pieces in P1G and over ten adjacent frequencies in a single 90-day record in P1H). The stretched depth-time scaled data were used to calculate frequency-stretched vertical wavenumber spectra (averaging over ten 9-day pieces for each record) using the conventional beamforming estimator. As desired, these were further averaged over relevant frequency or vertical wavenumber bands (as specified in the text).

Composite wind records from the LOTUS surface mooring buoy (when available) and National Weather Service synoptic maps (otherwise) were provided to us by Dr. R. Weller of W.H.O.I. These records are used here merely to indicate the intensity of local wind forcing and are inappropriate for use in calculating dynamic response to forcing because of inadequate temporal and/or spatial resolution.

3. The subinertial environment

Upper-ocean temporal variability at the LOTUS site is dominated by the growth and decay of the seasonal pycnocline and the passage of mesoscale eddies or Gulf Stream rings at scales longer than the inertial time scale. Both types of variability are evident in the daily-averaged potential density depth–time sections in Fig. 1. In the P1G record (Fig. 1a), stratification over the range profiled starts out as relatively weak in April [buoyancy frequency N is approximately 2.5 cycles per hour (cph)] and gradually strengthens, more so at the shallower depths profiled, until in July seasonal pycnocline daily average N values reach and exceed 10 cph (calculated over a 10 m interval). The development of the seasonal pycnocline is modulated at time scales of several days by the passage of mesoscale eddies and/or Gulf Stream rings. These cause pycnocline displacements of as much as a few tens of meters. In the P1H record, the pycnocline deepens and dissipates through the winter, starting with peak values $N \sim 10$ cph in November and reducing to $N \sim 3$–5 cph in January, capped by a mixed layer. As in the spring–summer record, pycnocline evolution is neither smooth nor monotonic, largely due to mesoscale variations. Typical variations in N are a factor of 5 or so in depth from the top of the pycnocline to the deepest depth profiled. Averaged over the 80–180 m depth range for which data pieces for spectral analysis in Table 1 defined, daily average N varies from 2.0 to 5.0 cph in P1G and 2.6 to 5.4 cph in P1H. These ranges suggest that application of WKBJ scaling and stretching is necessary to evaluate spectral contributions by short vertical scale internal waves in the LOTUS data.

Currents associated with the density variations attributed to mesoscale features in the records are substantial with reference to phase speeds of moderate to short internal waves. Progressive vector diagrams (see Eriksen 1987) indicate speeds of 0.5 m s^{-1} are maintained for a week or more throughout the profiling range on various occasions in each record. There are also weeklong intervals of currents less than 0.1 m s^{-1}.

4. Frequency spectra of horizontal current

The PCM profile time series may be treated as time series at an equally-spaced sequence of fixed depths. Autospectra of (temporally) clockwise and anticlockwise current components as a function of depth are plotted isometrically in Fig. 2 for P1G and P1H. The estimates at the lowest ("zeroth") frequency plotted in the P1G spectra are small as an artifact of piece-averaging whereas the P1H estimates are much higher at this frequency estimate because frequency rather than piece-averaging has been used to form them. The independent spectral estimates are plotted on a uniform grid corresponding to harmonics of 1 cycle per 9 days. Aside from the different treatment of the "zeroth" harmonic (plotted at a frequency 0.25 cycles/9 days

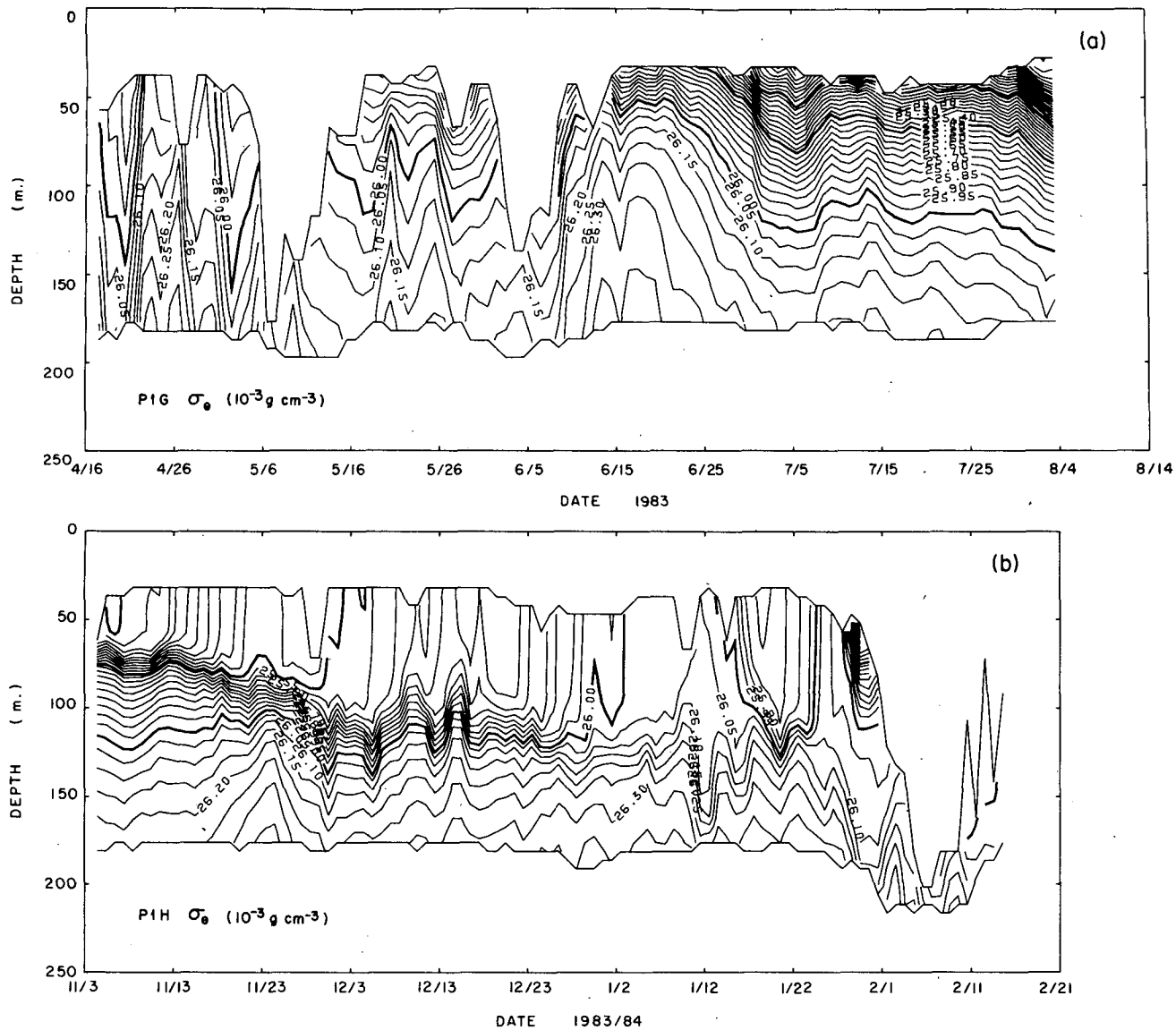

FIG. 1. Depth–time sections of daily-averaged potential density σ_θ from spring–summer (P1G) and fall–winter (P1H) records. Variations in profiling depth coverage are due to mooring motion. The domain contoured is limited to depth bins for which all six profiles possible in a given day were made.

= 0.00116 cph), spectral shape and levels differ considerably between the P1G and P1H records. Since the P1H spectra correspond more closely to what is observed deep in the ocean, they are discussed here first.

The P1H spectra (lower two panels of Fig. 2) indicate that much more clockwise motion is present at frequencies near (but above) the inertial frequency than at the higher frequencies resolved (approaching the Nyquist frequency, 0.125 cph) in this record. The 10th harmonic (11th frequency estimate plotted) corresponds to a band nearly centered on the inertial frequency. Whereas there is little depth dependence at low (subinertial) frequencies and near the Nyquist frequency, near-inertial energy drops by roughly a factor of 5 from 80 to 180 m depth (lower left panel, Fig. 2). Not only does the clockwise inertial peak change level over this short range of depths, but it shifts to higher frequency with increasing depth as can be seen by the nearly equal levels of the estimates in the 10th (inertial) and 11th harmonics for depths greater than about 150 m. The other prominent peak in the clockwise spectrum is at the semidiurnal tide. As expected for a boreal open ocean region over a flat bottom, the semidiurnal tide (whether barotropic or baroclinic) has clockwise polarization.

The dashed curves drawn in the left two panels of Fig. 2 correspond to the Garrett–Munk (Munk 1981, hereafter GM) prediction for the spectrum of clockwise

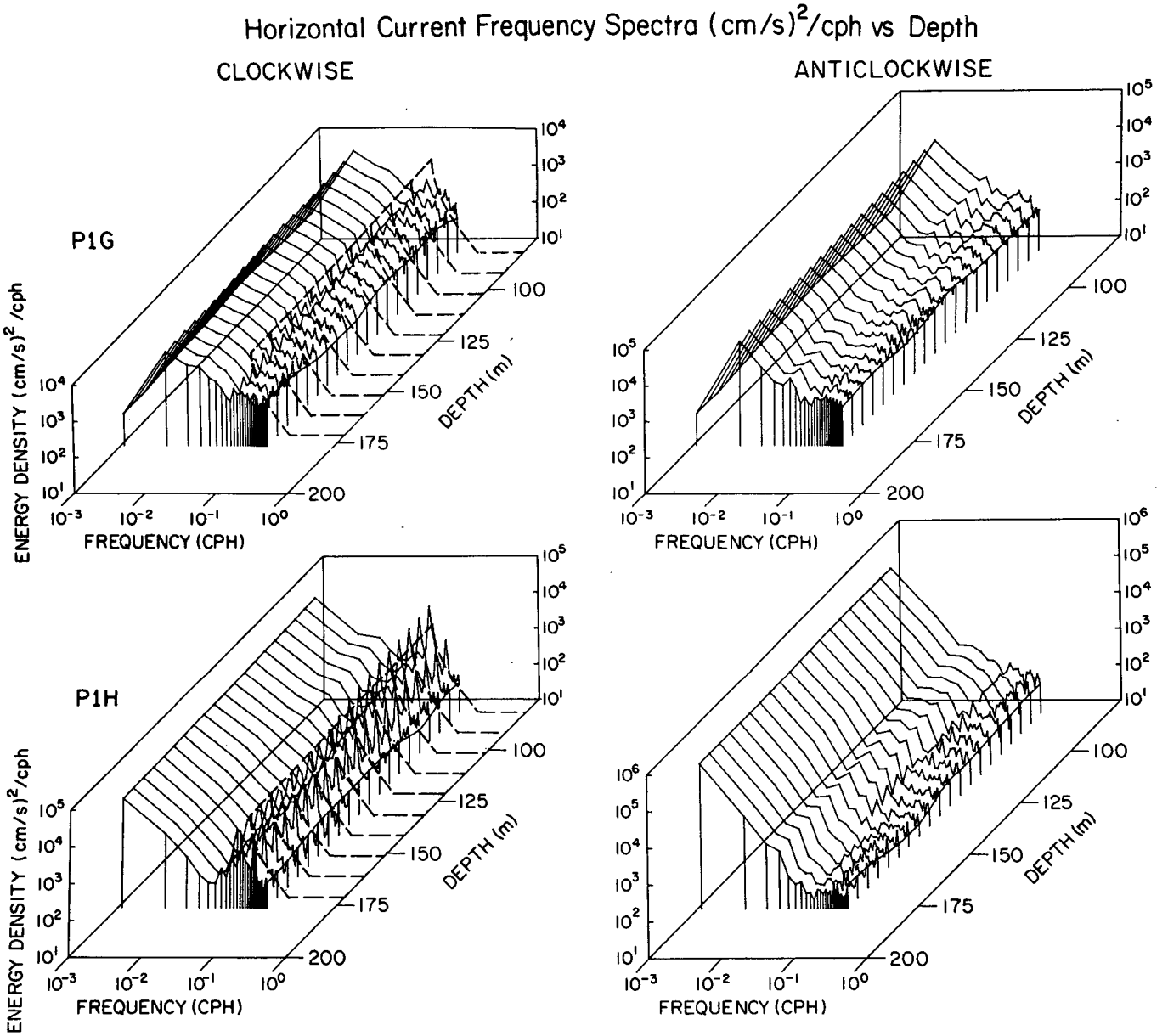

FIG. 2. Frequency spectra of clockwise and anticlockwise current components for individual depth bins for P1G and P1H. Spectral estimates are plotted on a frequency grid with 1 cycle/9 day bandwidth, starting with the "zeroth" estimate (plotted at 1.157×10^{-3} cph). The zeroth estimates differ substantially in P1G and P1H spectra because estimates were formed by averaging squared periodograms from ten 9-day records and averaging over ten adjacent squared Fourier coefficients from a single 90-day record, respectively. Intervals of 95% confidence for the (independent) estimates plotted are 2.09 to 0.59 times the estimate. The dashed curves overlaid on the clockwise spectra are the GM prediction divided by 3 (see text and Appendix).

motion adjusted downward by a factor of 3 in order to match the observed spectra (see the Appendix). These model spectra were computed by solving for the baroclinic mode shapes of horizontal current based on typical $N(z)$ profiles found at the LOTUS site and weighting their contribution according to $(j^2 + j_*^2)^{-1}$ where j is mode number and $j_* = 3$ according to GM. Since the low-mode shapes are most heavily weighted and they vary only slightly with depth over the top 180 m in spite of the existence of the seasonal pycnocline, the GM prediction is nearly depth independent over this range. With the exception of the semidiurnal tide (which is not modeled intentionally by GM), the GM spectral shape corresponds well to the P1H clockwise current frequency spectra (Fig. 2, lower left panel), which vary roughly as ω^{-2} for $\omega \gg f$ (where ω is frequency and f the inertial frequency). The correspondence for P1G is much poorer.

The top two panels in Fig. 2 indicate that not only is there at most only an anemic inertial peak in the clockwise spectrum of P1G, but the anticlockwise spectrum is nearly the same level even near the inertial frequency. Moreover, the clockwise energy at the higher frequencies resolved is a factor of 3 or so higher than in P1H. There is no prominent tidal peak in the P1G records; however energy in the tidal band is about the same as in the P1H record. That is, the tidal peak is obscured by the flatter, less circularly polarized spectrum of superinertial motions in P1G. The prominent spectral well at subinertial frequencies in the P1H clockwise spectra is not present in the P1G spectra, where spectral levels are a factor of 3–30 times higher over this range dominated by eddy fluctuations rather than internal waves. The GM model (dashed) curves in the upper left panel of Fig. 2 are identical to those in the lower left panel. By way of contrast with the observations, they emphasize how different the P1G spectral shape is from that of P1H as well as from GM. This shape is characterized by a much flatter shape in frequency ($\alpha\omega^{-1}$), a very weak inertial peak, and lack of clockwise polarization.

Although the P1G and P1H measurements were made less than 10 km apart, at the same depths, and with only three months between the end of the first and start of the second record, their spectra (based on 90 days of data from each record) differ substantially. Clearly, the GM spectral description is inadequate for even a three-month average in this location. A description of internal wave spectra temporal changes and possible relationships to environmental influences is presented next.

5. Temporal variations in internal wave band energy

To find explanations for why the frequency spectra calculated from the two 3-month records P1G and P1H differ so dramatically, it is necessary to make spectral estimates over shorter record pieces. Since the shortest piece for which the inertial and diurnal (tidal) frequencies can be distinguished is 9 days, the pieces defined in Table 1 were chosen to estimate internal wave variance. In order to account for the possibility that waves with scales short compared to low baroclinic mode waves contribute significantly to internal wave energy, current records were scaled and stretched as outlined in section 2 using the N profile appropriate to each piece. These records were then two-dimensionally Fourier transformed (in time and stretched depth), then averaged over all resolvable wavenumber bands (corresponding to −0.1 to 0.1 cpm true vertical wavenumber), and further averaged over appropriate frequency bands to attain additional statistical confidence. Based on the vertical separation over which current coherence drops to below 0.5 (typically 50 m), for the purpose of calculating confidence intervals, summing over all wavenumbers is roughly equivalent to doubling the number of independent estimates averaged. In the discussion which follows, spectra are computed over three (overlapping) groups of frequency estimates: 1) the 10th harmonic, centered at 1/21.6 cph, encompassing $0.94f$–$1.04f$ (periods 22.7–20.6 h); 2) harmonics 10–16 encompassing $0.94f$–$1.64f$ (periods 22.7–13.1 h); and 3) harmonics 10–26 encompassing $0.94f$–$2.63f$ (periods 22.7–8.2 h). These three bands encompass the inertial, inertial to (but not including) semidiurnal tides, and inertial to Nyquist frequencies, respectively.

Time series of energy summed over these frequency bands indicate substantial differences in the relative contributions of different bands to the total as well as variation in the total by roughly a decade. The estimated variance in both current components together (labeled "twice horizontal kinetic energy") for each of the twenty 9-day pieces (P1G and P1H) is plotted in Fig. 3. Although the P1G inertial band energy estimates tend to be less than the P1H estimates for this band ($0.94f$–$1.04f$, the bottom curves in Fig. 3), there is both substantial overlap and the 95% confidence intervals are large. The band $0.94f$–$1.64f$ is much more energetic than the inertial band in P1G, but the two are not so disparate in P1H, demonstrating the tendency for the inertial peak to make the dominant contribution to variance in the fall–winter, but not in the

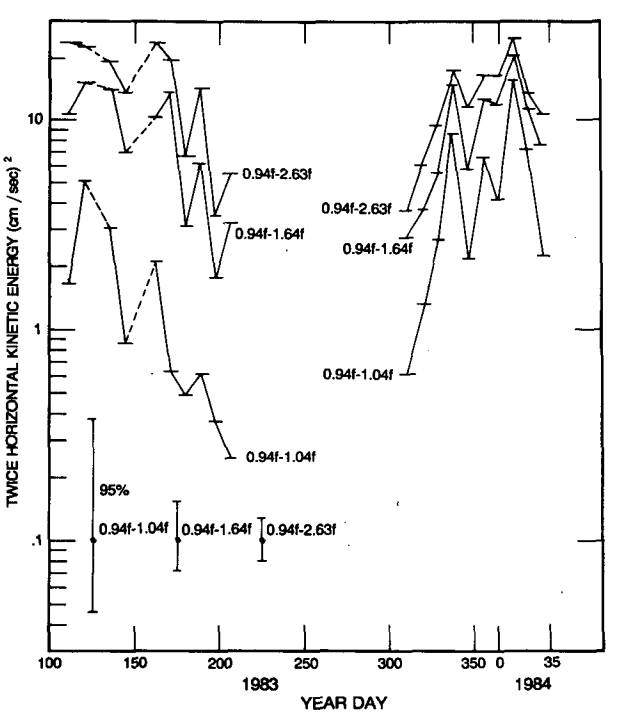

FIG. 3. Time series of scaled horizontal current variance from 9-day data pieces summed over stretched vertical wavenumber and over frequency bands as labeled. See text for details. The first and last ten estimates correspond to P1G and P1H data pieces defined in Table 1.

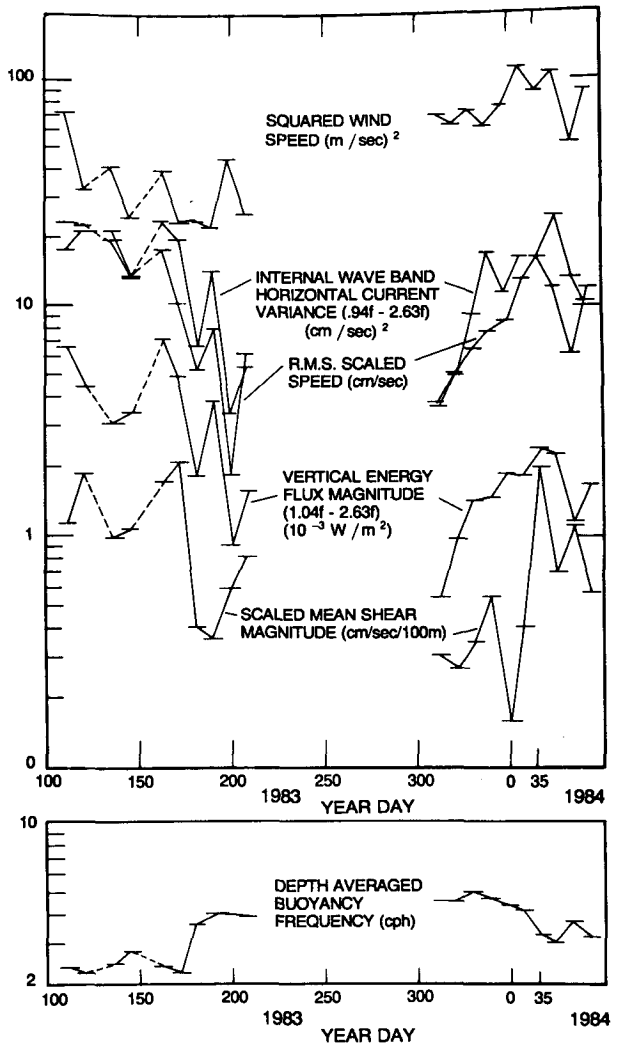

FIG. 4. Time series of internal wave scaled current variance plotted as in Fig. 3 together with estimates of vertical energy flux magnitude, squared wind speed, rms-scaled subinertial frequency speed, scaled mean-shear magnitude, and buoyancy frequency. See text for detailed definitions of these quantities.

spring–summer record. Summing over the full band from inertial to Nyquist frequencies does little to increase the total energy in either P1G or P1H, indicating that temporal fluctuations in total energy are dominated by the low frequency portion of the internal wave band (e.g., $0.94f$–$1.64f$).

Other quantities in addition to internal wave band current variance exhibit substantial variation in the P1G and P1H records. Estimates of the magnitude of internal-wave vertical energy flux resolvable over the depth range profiled vary in a manner similar to current variance (where the energy flux magnitude is calculated as the sum of the absolute values of upward and downward energy density times group velocity). Several environmental indices are plotted together with internal wave energy and energy flux in Fig. 4. They are the rms-scaled speed, scaled mean shear magnitude, depth-averaged N, and squared wind speed (sometimes referred to as "pseudostress") calculated for each 9-day data piece. Neither depth averaged N nor squared wind speed are correlated with either measure of internal wave activity as can be seen in the time series of Fig. 4. Since WKBJ scaled, stretched time series are used to calculate the internal wave statistics in these plots it is not surprising that these exhibit no correlation to buoyancy frequency. In contrast, although 9-day average wind stress more than doubles between the spring–summer and fall–winter seasons, internal wave energy (current variance) over these two periods is roughly the same. The time series which is best correlated with internal wave energy in Fig. 4 is rms-scaled speed, defined as the square root of the sum of scaled 9-day mean speed squared and subinertial-scaled current variance. Scaled 9-day mean shear magnitude is also correlated with internal wave energy, but to a lesser extent. Since much of the subinertial variability is presumably due to mesoscale eddies (whose vertical structure is a combination of barotropic and primarily the first baroclinic mode), it is not surprising that scaled 9-day mean shear is so similar to rms-scaled speed (despite neglect of the contribution of the subinertial portion of the shear spectrum).

The strong correlation of low frequency internal wave band current variance with rms-scaled speed is illustrated by the (logarithmic) scatter plot in Fig. 5. The sample correlations for P1G, P1H and all twenty 9-day estimates together are 0.93, 0.79 and 0.87, re-

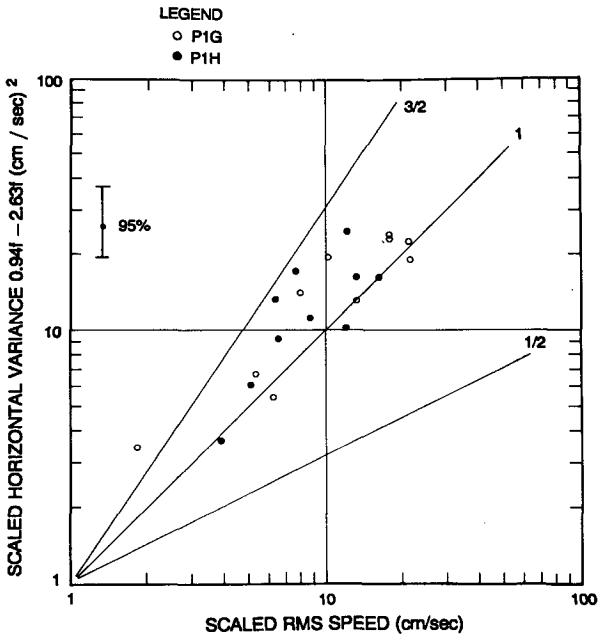

FIG. 5. Scatter plot of internal wave scaled current variance vs rms-scaled speed for the same 9-day pieces used in Figs. 3 and 4. Power law dependences of 1.5, 1.0 and 0.5 are plotted for reference.

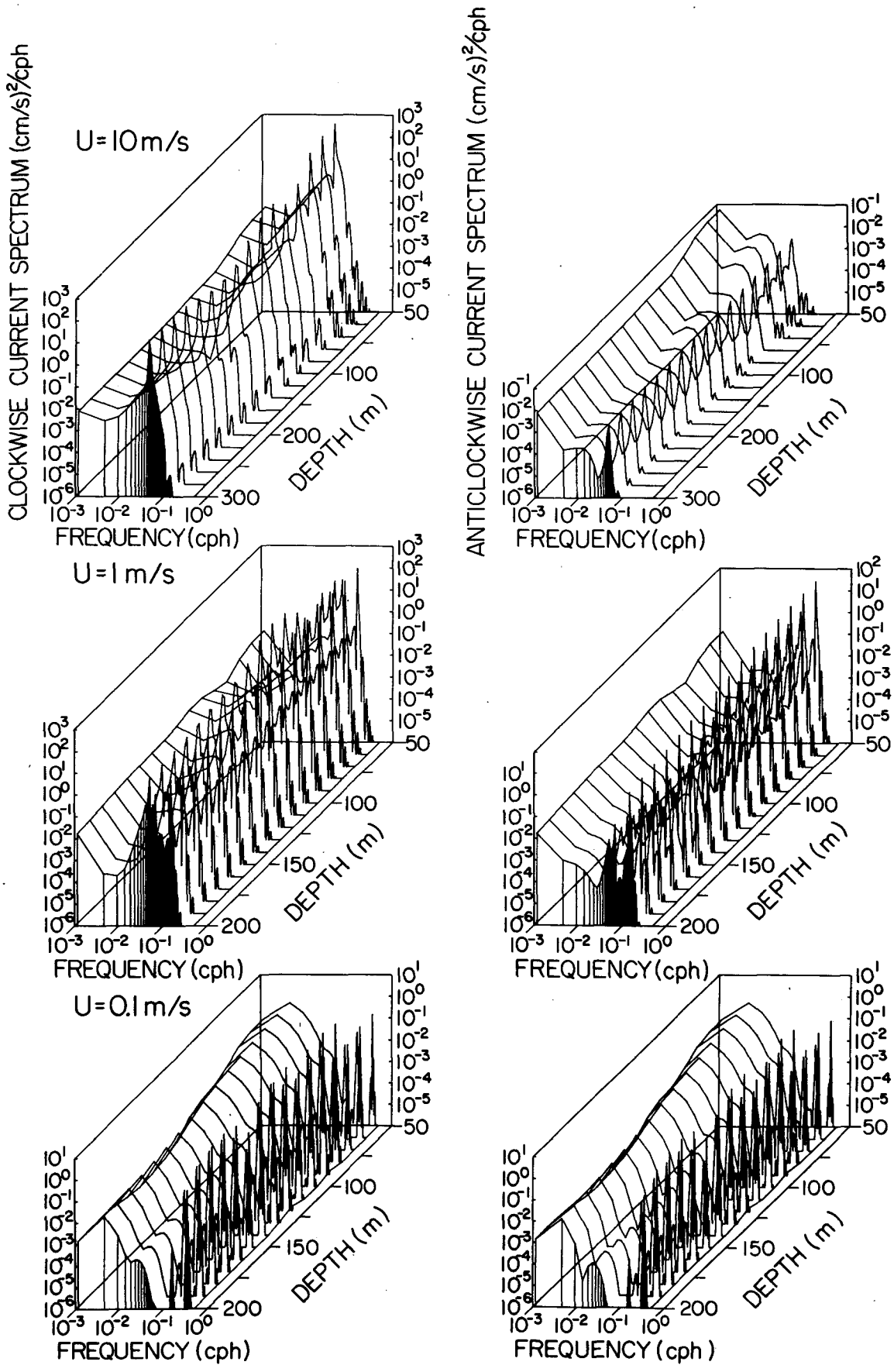
CLOCKWISE CURRENT SPECTRUM (cm/s)²/cph
ANTICLOCKWISE CURRENT SPECTRUM (cm/s)²/cph
U=10 m/s
U=1 m/s
U=0.1 m/s
DEPTH (m)
FREQUENCY (cph)

spectively, which are all significantly nonzero at 95% confidence. [These are correlations using the model variance = $a(\text{speed})^b$ calculated as a least squares fit to log(variance) = log$a$ + b log(speed).] Taking P1G and P1H estimates together, the sample slope $b = 0.85$ which has uncertainty ±26% (Bendat and Piersol 1971). This slope is indistinguishable from 1.0 but distinguishable from 0.5 or 2, the slopes drawn for reference in Fig. 5. The robust correlation suggests strongly that internal wave energy is modulated by subinertial currents. A model for this relationship is presented in section 7.

6. Direct forcing by propagating winds

The principal deviation of the P1H frequency spectra from the GM spectral shape described in section 4 is depth dependence of inertial energy, including a "blue shift" of the inertial peak to higher frequency with increasing depth. These features are characteristic of model ocean response to the stress field of moving wind systems. One way to characterize the wind field is as a collection of moving systems, as indicated by synoptic weather maps for the LOTUS region (R. Weller, personal communication). Each system will generate its own wake and the resulting collection of wakes can be expected to mask the identity of individual wakes. However, since each wake characteristically exhibits a blue shift with depth as baroclinic modes disperse, this feature will not be lost by interference. Calculations in this section using typical storm translation speeds indicate that the degree of blue shift predicted is consistent with the LOTUS observations.

The model of Kundu and Thomson (1985) is useful to illustrate the depth dependence of near-inertial response, to which the reader is referred for details. This model parameterizes wind stress as a body force applied to a surface mixed layer. This stress divergence pattern is projected onto the various available free wave modes. In the model, an atmospheric front is idealized as a translating jump in wind stress, a line source moving at speed U. The response is composed of barotropic and baroclinic modes which are standing waves or evanescent waves in the frame of reference of and with respect to the moving stress source. The waves are standing (sinusoidal) or evanescent (exponentially decaying) with distance from the front depending on whether the characteristic eigenspeed c_n of each vertical mode is slower or faster than U (where each wave has real or imaginary frequency $\omega_n = f(1 - c_n^2/U^2)^{-1/2}$ and wavenumber $k_n = \omega_n/U$). Although there is no dissipation in this model, wake amplitudes remain finite because the line source forcing is considered to travel an infinitely long distance and carry with it a wake for an infinitely long time related by the fixed rate of advance U. The amplitude of the response from mode n is proportional to ω_n and to the projection of the vertical distribution of the vertical gradient of stress on this mode. For waves with minimum phase speed c_n far less than the translation speed U, response is nearly at, but slightly above, the inertial frequency. At speeds comparable to c_n, the response is resonant and at frequency $\omega_n \gg f$.

In general, midlatitude wind systems tend to travel fast compared to the baroclinic mode eigenspeeds c_n of the deep ocean ($c_n \sim \bar{N}D/n\pi$ where $\bar{N} = \int_{-D}^{0} N dz$ and D is ocean depth), thus the principal forced response is at frequencies slightly greater than inertial independent of the spatial structure of the wind (as long as its components have $U \gg c_n$). In the Kundu and Thomson model, baroclinic response is composed of forced vertical modes which add near the front itself to produce nearly pure inertial motion at the surface and vanishing flow at depth. These modes each have different frequencies ω_n and wavenumbers k_n that interfere with increasing time and distance from the front. The interference contributes to the appearance of upward phase propagation (corresponding to downward energy flux) and depth dependence in the frequency spectrum of motions. A more complicated wind stress pattern merely complicates the response, yet will have qualitatively the same response: a modulation of the inertial peak with depth and a (blue) shift to higher frequencies.

An $N(z)$ profile from the LOTUS site and typical frontal speeds U can be used to calculate model autospectra as at different depths to compare with the observed spectra (Fig. 2). To construct model spectra for this comparison, a $9d$ wake behind a model front was sampled in depth and time on the identical grid that PCM measurements in LOTUS were collected. Model frequency spectra from these deterministic simulated data were estimated as the squared Fourier coefficients of time series at each depth evaluated. These are plotted in Fig. 6 for $U = 10$, 1 and 0.1 m s^{-1} in the same manner as the observed spectra. For a front which travels faster than all the baroclinic mode eigenspeeds, strictly inertial band amplitudes tend to decay with depth (top left panel, Fig. 6), even though response is sharply peaked near the inertial frequency. The near-inertial band also broadens in the direction of higher frequency (i.e., undergoes a "blue shift"). The clockwise spectrum dominates the anticlockwise spectrum near the inertial frequency and less so at higher fre-

FIG. 6. Model clockwise and anticlockwise current frequency spectra for internal waves forced by a step line source of stress of 0.1 Pa moving at speeds $U = 10$, 1.0 and 0.1 m s^{-1} (top, middle, and lower panels). Spectra were estimated from a 9-day simulated data piece starting at the time of frontal passage for each of the three cases. Calculations used vertical modes calculated from a spring–summer average $N(z)$ profile for the LOTUS site. Frequency grid is identical to that in Fig. 2.

quencies as expected for internal waves in a resting ocean. For slower moving fronts ($U = 1$ or 0.1 m s^{-1}, middle and lower panels, Fig. 6), modes are forced at higher frequencies than near-inertial. The biggest responses are for those modes which have eigenspeed c_n very close to U.

The overall character of the forced spectra in Fig. 6 is that they are rather sharp. They are so sharp that sidelobes due to the finite record length Fourier transformed are evident in many cases (particularly prominent, for example, in spectra at 50–70 m depth in the $U = 10$ m s^{-1} case, top panels, Fig. 6). For the observed superinertial continuum spectrum to be explained as wind-forced waves, an unrealistically special combination of translating wind stress patterns would be required, hence a forced wave model is realistic only near the inertial frequency. A model of wind-forced waves in an otherwise resting ocean is also incapable of explaining the severe changes in current component polarization which were observed in LOTUS. A translating wind stress does produce, however, plausibly realistic depth dependence of near-inertial motions. Although the precise form of this depth dependence is dependent on the details of the forcing and the speeds of the available baroclinic modes, the superposition of several internal wave wakes still exhibits inertial peak decay and blue shift with depth. Superposition of different wakes traveling at different speeds and in different directions will tend to reduce coherence between local wind and subsurface currents, yet retain this tendency in autospectra for inertial peak decay and blue shift with depth. Kundu (1986) extended the Kundu and Thomson (1985) work to consider a uniformly propagating wind system and recognized in conclusion that the assumption of uniform translation speed and direction leads to unrealistically large near-inertial internal wave coherence scales, both vertically and horizontally.

The stronger wind stresses in winter than in summer (see Fig. 4) coupled with comparable or weaker currents are a plausible explanation for the relative prominence of the observed near-inertial peak and its depth dependence in the P1H records. Conversely, the lack of inertial peak in the P1G records is due to a combination of weak winds and strong currents. The model spectra of Fig. 6 are calculated for a single line source with a stress jump of 0.1 Pa (1 dyn cm^{-2}). The inertial peaks are a factor of 10–25 smaller than observed, indicating that some combination of stronger stress jumps (values as large as 1 Pa are plausible) and superposition of several frontal passages is sufficient to account for the observed peak heights. In order to explain other features of the observed spectra, a different model is required.

7. Local modulation by subinertial currents

The observed correlation between internal wave energy and subinertial current speed suggests the possibility that wave–mean flow interaction contributes to internal wave variability. The detailed structure of subinertial currents is complicated and was, for the purposes of calculating ray traces of internal waves, inadequately observed during LOTUS. Nevertheless, the tendency of mesoscale currents to modulate the internal wave spectrum through simple wave–mean flow interaction can be examined by considering an illustrative example. For simplicity, the vertical shear of mesoscale variability is neglected and only horizontal shear retained to isolate its effects. This is in contrast to the more general situations considered by Olbers (1981) and Kunze (1985) where single ray calculations in fully baroclinic flows require consideration of wave–mean flow interaction in three dimensions. Here, the interaction of a parallel barotropic flow with a wave field specified by the GM spectrum is explored as a tendency calculation for spectral modulation. It neglects acceleration of the mean flow by internal waves, assumes relative vorticity of mean flows can be neglected relative to planetary vorticity, ignores the effects of waves reflected (refracted back) by the current, neglects effects of nonuniform stratification, and neglects the effects of vertical shear. (Some of these effects have been considered by others and their relevance is discussed in section 9.) Despite these considerable simplifications, the resulting model spectra resemble observed spectra in several respects.

Consider a parallel barotropic flow $\mathbf{V} = U(y)\mathbf{x}$ where $\mathbf{x}$ is the Cartesian unit vector in the positive x direction. Without loss of generality, take $U(0) = 0$, specify the internal wave spectrum by GM (see the Appendix) at $y = 0$, and consider only waves propagating into $y > 0$. Since reflection and critical layers are neglected, the spectrum and current $U(y)$ in $y < 0$ does not affect conditions in the half-plane $y \geqslant 0$. Following the treatment of Lighthill, 1978 (Chapter 4) each internal wave component of the spectrum prescribed at $y = 0$ can be traced into the parallel shear flow according to the rules of ray tracing. For this particular case, the intrinsic frequency ω_r (where r refers to a frame of reference at rest relative to the local mean flow) is a spatial function of y alone if the stratification N and the current U are specified as depth independent, for simplicity. Then internal waves obey the dispersion relation

$$\frac{m^2}{k^2 + l^2(y)} = \frac{N^2 - \omega_r^2(k, l(y), m, y)}{\omega_r^2(k, l(y), m, y) - f^2} \tag{1}$$

and ω_r is related to frequency ω in a resting frame by

$$\omega = kU(y) + \omega_r(k, l(y), m, y) \tag{2}$$

where k, l and m are wavenumber components in the x, y and z directions. Whereas ω, k and m are constant along rays, $l(y)$ and ω_r change along a ray according to $dl/dt = -\partial\omega_r/\partial y$ and

$$d\omega_r/dt = -\frac{\partial\omega_r}{\partial l} k \frac{\partial U}{\partial y}$$

where d/dt represents the derivative following a ray. Ray directions are specified by

$$\frac{dz}{dy} = \frac{\partial\omega_r}{\partial m}\Big/\frac{\partial\omega_r}{\partial l}, \quad \frac{dx}{dy} = \left(U(y) + \frac{\partial\omega_r}{dk}\right)\Big/\frac{\partial\omega_r}{\partial m} \tag{3}$$

which are functions only of one spatial coordinate, y. Hence sections of a ray tube past any vertical plane parallel to the mean flow have the same area so that the wave field is said to be solenoidal. Then average wave energy per unit volume E_r is specified by

$$\frac{\partial}{\partial y}\left(E_r\frac{\partial\omega_r}{\partial l}\Big/\omega_r\right) = 0 \tag{4}$$

so that the cross-current component of wave action flux is constant in this problem. If E is the energy of a wave component at $y = 0$, then the energy within the mean current E_r is given through the ratio

$$\frac{E_r}{E} = \frac{\omega_r}{\omega}\frac{\partial\omega/\partial l}{\partial\omega_r/\partial l}. \tag{5}$$

Conveniently, this ratio can be evaluated without performing a ray trace. That is, energy E_r depends only on the local value of current $U(y)$, not on its spatial structure.

A wave with frequency ω, vertical wavenumber m and azimuth ϕ (where $\phi = \tan^{-1}k/l_0$ and l_0 is the cross-current wavenumber at $y = 0$) changes azimuth ϕ and cross-current wavenumber l according to

$$\tan^2\phi_r = \tan^2\phi + (\omega_r^2 - \omega^2) \times (N^2 - \omega_r^2)^{-1}(N^2 - f^2)(\omega^2 - f^2)^{-1}/\cos^2\phi \tag{6}$$

$$l^2(y) = l_0^2 + m^2(\omega_r^2 - \omega^2) \times (N^2 - \omega_r^2)^{-1}(N^2 - f^2)(N^2 - \omega^2)^{-1}. \tag{7}$$

Its cross-current group velocity is given by

$$\frac{\partial\omega_r}{\partial l} = (\omega_r^2 - f^2)^{1/2}(N^2 - \omega_r^2)^{3/2} \times \omega_r^{-1}(N^2 - f^2)^{-1}m^{-1}\sin\phi_r \tag{8}$$

so that the ratio (5) can be written as

$$\frac{E_r}{E} = \frac{(\omega^2 - f^2)^{1/2}(N^2 - \omega^2)^{3/2}\sin\phi\omega_r^2}{(\omega_r^2 - f^2)^{1/2}(N^2 - \omega_r^2)^{3/2}\sin\phi_r\omega^2}. \tag{9}$$

Together, the Eqs. (1), (2), (6) and (9) specify the energy density of a wave component at arbitrary current speed $U(y)$ based on its energy, wavenumber, and frequency at $y = 0$ as long as it has not entered a critical layer or undergone reflection. Reflection occurs for waves entering flow with a downstream propagation component where l is reduced through zero according to Eq. (7) at a point where ω_r is reduced to

$$\omega_c = \left[\omega^2 - (\omega^2 - f^2)\left(\frac{m^2}{m^2 + k^2}\right)\sin^2\phi\right]^{1/2} \tag{10}$$

where $f \leqslant \omega_c \leqslant \omega$. A critical layer is approached when $\omega_r \to N$ so that $l \to \infty$ according to (7). In contrast to the more familiar case of an internal wave propagating vertically in a parallel vertically sheared flow (discussed by Lighthill), in the case of parallel horizontally sheared flow, waves with an upstream component of propagation turn across the direction of flow becoming shorter and of higher intrinsic frequency as they approach a critical layer. Conversely, waves with a downstream component of propagation turn toward advection parallel to the flow as their intrinsic frequency reduces to the value given in (10) whereupon they refract back out of the flow ("reflect").

Before summing a full spectrum of linear waves, it is instructive to consider amplification of individual rays with arbitrary incidence azimuth ϕ, frequency and Doppler shift. Doppler shift can be scaled by the ray slope in the vertical plane parallel to the mean flow k/m so that the variables ϕ, ω/f and mU/f are independent. Although other choices are possible, this one is convenient for use with an energy spectrum specified in quiet water (i.e., at $y = 0$) as a function of ω, m and ϕ. Examples of the ratio E_r/E for fixed ϕ as a function of ω/f and mU/f are given in Fig. 7. The ratio is contoured in decibels for the domain $\omega_c \leqslant \omega_r \leqslant \omega$ for $0° \leqslant \phi \leqslant 90°$ (downstream incidence) and $\omega \leqslant \omega_r \leqslant N$ for $90° \leqslant \phi \leqslant 180°$ (upstream incidence). Additionally, the curve $\omega_r = f$ is plotted outside the contoured domain for downstream incidence. As the expression (9) and the plots indicate, energy tends to increase as $\omega_r \to \omega_c$ and even more rapidly as $\omega_r \to N$. (In the plots, $\omega_r \to \omega_c$ and $\omega_r \to N$ for fixed ω as mU/f increases toward the edge of the contoured domains.) The ratio is less than unity (negative contours in Fig. 7) for certain regions of frequency-Doppler shift space, notably those for which Eq. (9) is dominated by the trigonometric term $\sin\phi$.

The change in polarization which waves develop through interaction with the mean flow can be calculated from the spectra S_- and S_+ of clockwise and anticlockwise horizontal current components. These are given by

$$S_- = \tfrac{1}{2}(1 + f/\omega_r)^2E_r \tag{11a}$$

$$S_+ = \tfrac{1}{2}(1 - f/\omega_r)^2E_r. \tag{11b}$$

These functions are plotted for $\phi = 45°$ and $135°$ in Fig. 8. Although there is little difference in amplification of downstream incidence (upper panels), upstream incidence leads to substantially higher amplification of the anticlockwise than the clockwise spectrum as $\omega_r \to N$ (lower panels). This is because waves of a given frequency ω are more linearly polarized when Doppler shifted to higher intrinsic frequency ω_r than waves Doppler shifted to lower intrinsic frequency. This behavior accounts for horizontal current spectra being less circularly polarized for high vertical wavenumber

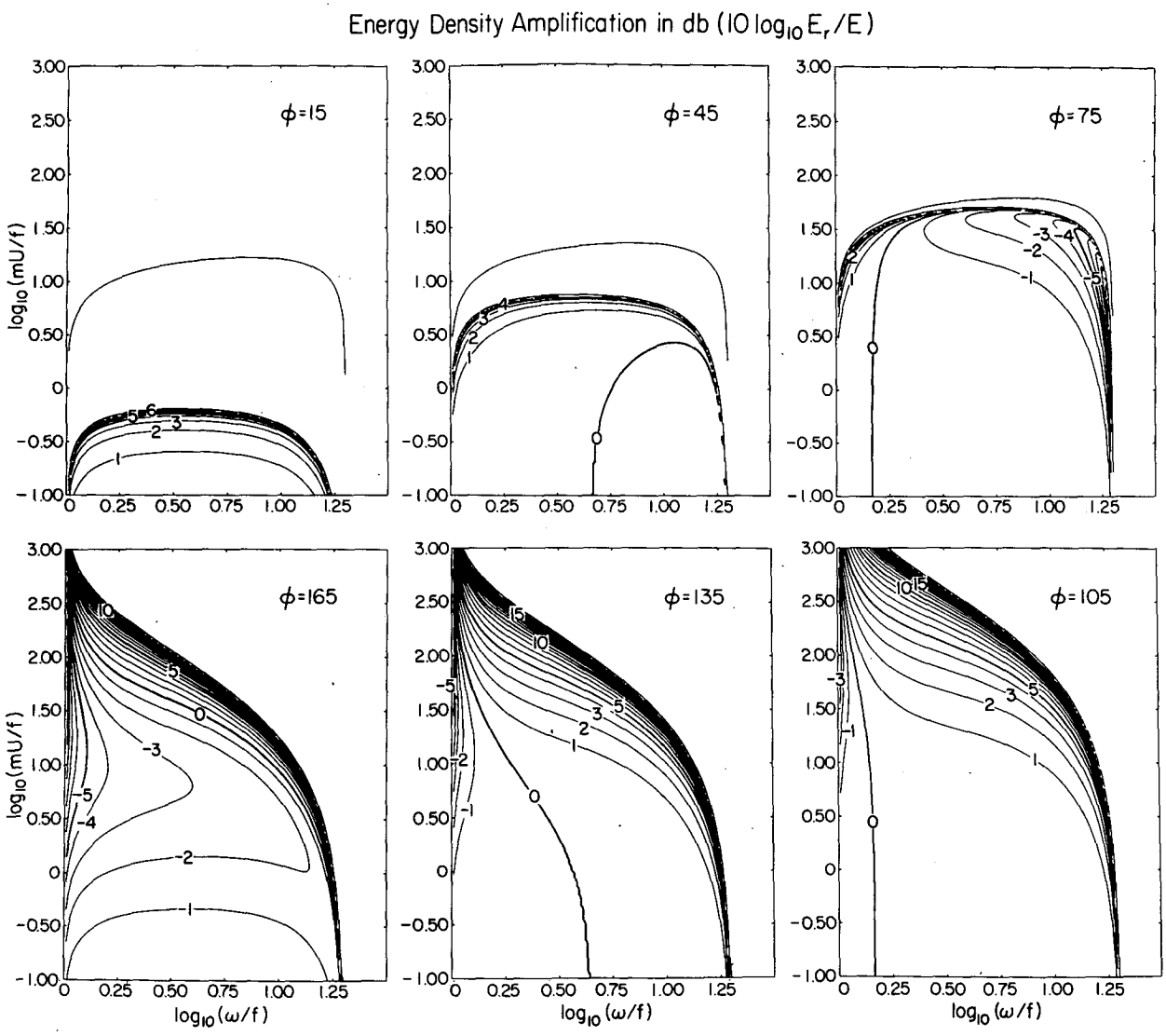

FIG. 7. Amplification ratios E_r/E plotted in db for scaled Doppler shift mU/f vs scaled frequency ω/f. Azimuths $\phi = 15°$, 45° and 75° correspond to downstream and $\phi = 105°$, 135°, 165° correspond to upstream rays. The $\phi = 90°$ (purely cross-stream) ray is unamplified (not shown).

waves or high current than for low vertical wavenumber waves or weaker current.

The relations (9) and (11) can be used to evaluate the distortion of a full spectrum of internal waves by parallel horizontally sheared flow. If the incident spectrum is given as the GM spectrum as defined in the Appendix but restricted to azimuths $0 < \phi < 180°$ (those waves which propagate into the half plane $y > 0$), the spectra of clockwise and anticlockwise current components appear in Fig. 9. The top panels of this figure, labeled $U = 0$, give the GM spectrum as a function of vertical mode number and frequency. In the center and bottom pairs of panels, the spectra for commonly occurring current strengths are plotted. These calculations omit any waves which would have undergone reflection (i.e., $\omega_r \leq \omega_c$) or any waves which would have approached critical layers (i.e., $\omega_r \geq N$). Hence this calculation is really a tendency calculation, arguably taken beyond validity to illustrate the qualitative effects of a weakly sheared parallel flow. The spectra for $U = 5$ and $U = 50$ cm s^{-1} exhibit both a spiky appearance and regular steps down at higher mode numbers because they are evaluated on a discrete grid of azimuths ($\phi = 5°, 15°, 25°, \cdots, 175°$). The joint frequency–wavenumber evaluations in Fig. 9 are also summed across frequency and wavenumber to form wavenumber and frequency spectra, respectively. These are plotted as curves in the planes of the panels upon which the axes are drawn in the figure.

The general character of distortion of the GM spec-

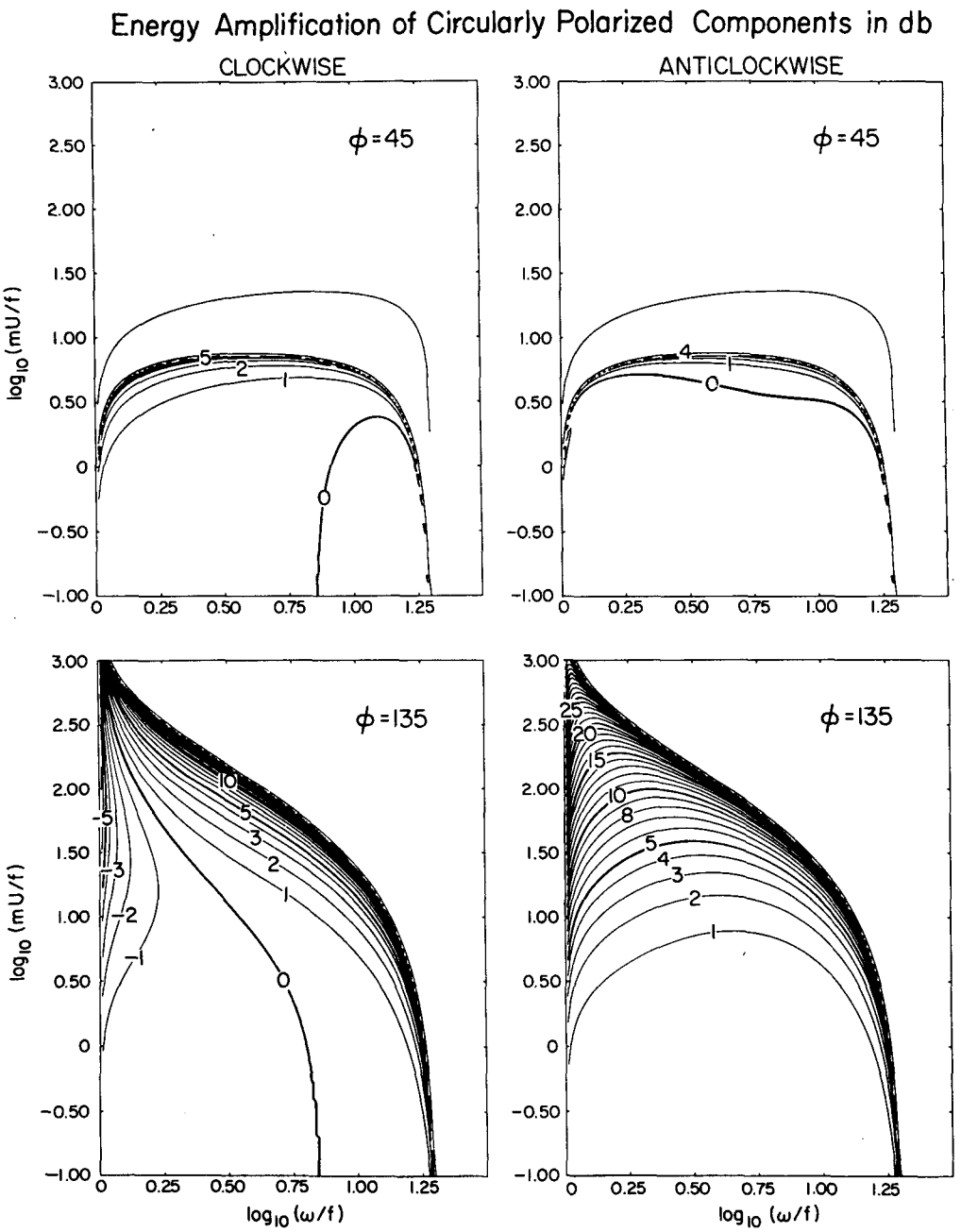

FIG. 8. Amplification ratios of clockwise and anticlockwise spectral components plotted as in Fig. 7 but for two azimuths only. The anticlockwise component of upstream rays is preferentially amplified, leading to a reduction of clockwise polarization for higher Doppler shift.

trum by simple parallel horizontally sheared flow is demonstrated by the calculations plotted in Fig. 9. Since expressions with singularities are evaluated on a discrete grid in ω, m and ϕ in the figure, the detailed structure of the resulting spectra is unimportant. The important features are that only the high frequency–high vertical mode portion of the spectrum is changed substantially for weak current ($U = 5$ cm s^{-1}) but virtually all of the high vertical mode portion of the spectrum is changed by a moderate current ($U = 50$ cm s^{-1}, a speed observed in LOTUS). The effect is to whiten and augment the (originally red) frequency spectrum and do the same for the wavenumber spectrum. Moreover, the frequency spectrum of anticlockwise current approaches that of the clockwise component at moderate current. As described in sections

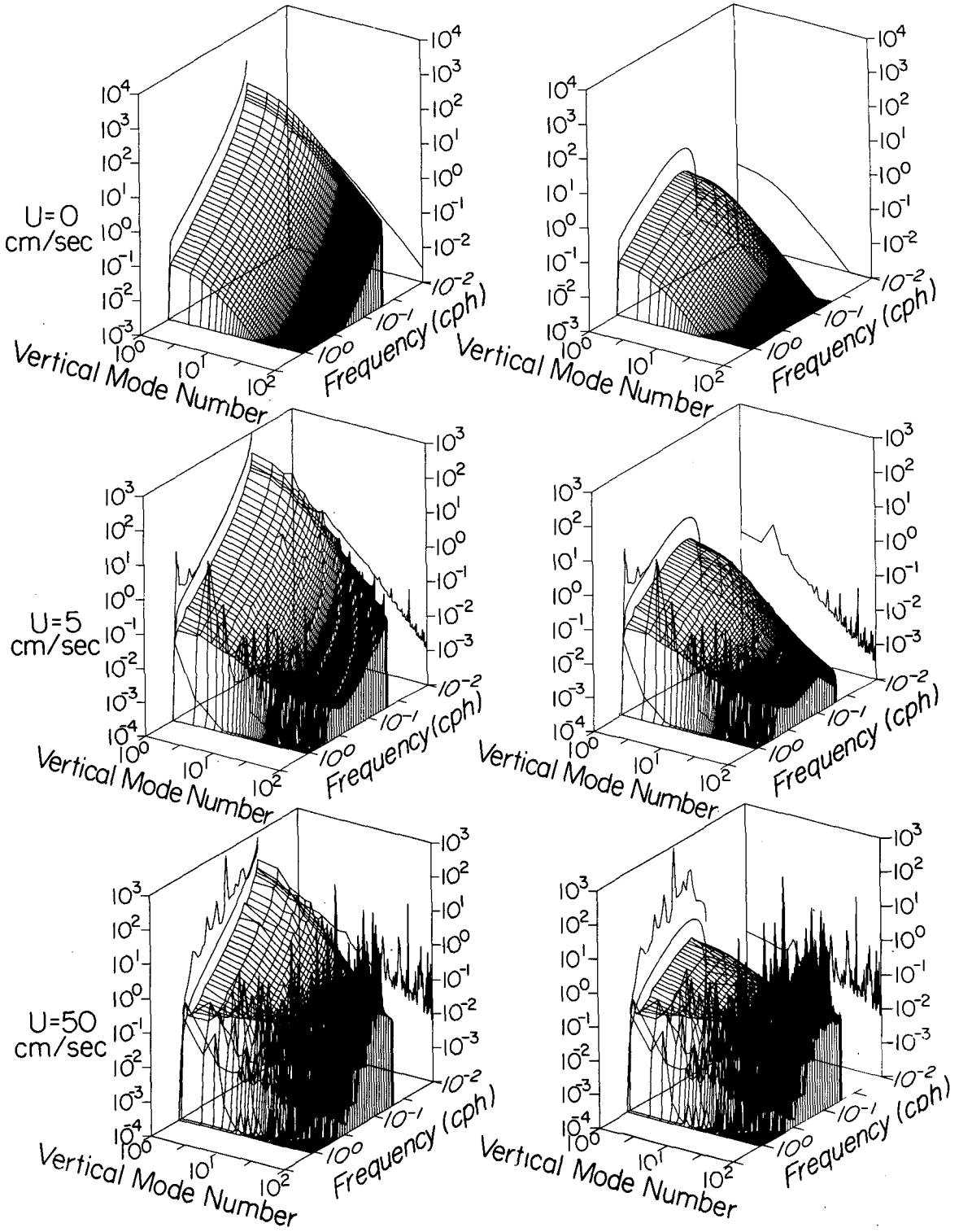

FIG. 9. Model clockwise and anticlockwise current frequency–vertical wavenumber spectra for quiet water $U = 0$ (the GM spectrum) (top panels) and Doppler shifted by propagation into a parallel horizontal shear flow with $U = 5$ and 50 cm s^{-1} (middle and lower panels). Single curves drawn in the plans at the rear of each panel give the frequency and vertical wavenumber spectra. See text for details of the calculation.

4 and 5, the prominent differences between internal-wave frequency spectra for conditions of low and high subinertial current variance (i.e., P1H vs P1G) are just these: a more energetic and less circularly polarized spectrum for higher current. The magnitude of the energy and slope changes predicted by this model calculation are comparable to those observed, once the calculations are smoothed in frequency to average over some spikiness in the evaluation. Smoothing over the spikiness of the vertical wavenumber spectra predicted by the model at high mode number (higher than about 10) gives a flatter and more energetic spectrum when subinertial currents are moderately strong (e.g., $U = 50$ cm s^{-1}). The tendency for a flatter wavenumber spectrum and weaker circular polarization at higher vertical wavenumber and during periods of high current is also a feature of the observations, as shown next.

8. Observed frequency–wavenumber spectra

Being profile time series, the PCM data allow estimation of joint frequency–vertical wavenumber spectra. As with the frequency spectra, estimates of the joint spectra from the P1G and P1H records differ somewhat. In addition, spectra from both records differ from the form assumed by Garrett and Munk (Munk 1981).

Estimates of joint frequency–vertical wavenumber spectra for current are resolvable only in a narrow band of vertical wavenumbers in the PCM records, barely more than a decade from 0.001 to 0.011 cpsm (both upward and downward). These were estimated by calculating a two-dimensional periodogram for each 9-day piece of stretched profiles and averaging both over ten pieces and over several frequency bands. Three broad frequency bands were chosen, corresponding to those discussed in section 5. These are a superinertial, a semidiurnal tidal, and a supertidal band defined by averaging over estimates centered at 10–16, 17–19, and 20–26 cycles per 9 days, respectively. The boundaries of these bands are at $0.94f$, $1.64f$, $1.94f$ and $2.63f$ corresponding to periods of 22.7, 13.1, 11.1 and 8.2 h just as in the discussion of temporal variations (section 5). The superinertial and supertidal bands were chosen also to have identical frequency bandwidth (0.0324 cph) so that the variances contained in them can be compared conveniently.

Superinertial band wavenumber spectra indicate that the excess of clockwise over anticlockwise energy found in frequency spectra is concentrated at the lower wavenumbers resolvable in PCM records (Fig. 10, top panels), as predicted by the model in the previous section. This tendency is particularly apparent in the P1H record, but can be seen in the P1G record as well. Although the clockwise and anticlockwise spectra differ from one another by a decade or more in P1H but only a factor of two or so in P1G, total energy in the two records in this band is about the same. Both records show more energy in upward wavenumbers, corresponding to net downward energy propagation (heavy vs light curves, Fig. 10, top panels). The magnitude of this excess is about a factor of two at all wavenumbers for P1G but mainly at low wavenumbers for P1H. In both records the dominant wavenumber slope is roughly -2 in this superinertial band.

The wavenumber spectra in the semidiurnal tidal band exhibit a similar, but less pronounced difference in polarization between P1G and P1H records (middle panels, Fig. 10) and have somewhat flatter wavenumber slopes (between -2 and -1). In contrast to the superinertial band spectra, the P1G tidal band total energy is greater than that of P1H. Also unlike the superinertial band, the semidiurnal tidal band P1H upward and downward wavenumber spectra are nearly equal while those for P1G are not (although less different than in the superinertial band).

Wavenumber spectra in the supertidal band indicate negligible circular polarization in both records, similar spectral slopes (roughly -1, which is flatter than in the two lower frequency bands), but roughly a factor of 4 more energy in the P1G record (lower panels, Fig. 10). In addition, the P1G spectra indicate a small but significant excess in downward energy flux whereas the P1H spectra do not.

The GM internal wave spectra assume that the wave field is both vertically symmetric and has a vertical wavenumber shape which is invariant in frequency. Although these assumptions are supported by many observations in the deep ocean, the LOTUS records do not support these tenets. Although the GM model is not intended as a description of the near-inertial part of the internal wave spectrum, it is for this part that the GM wavenumber shape best matches what is observed in the range of wavenumbers observable in the LOTUS PCM records. At higher frequencies, the observed wavenumber shape is substantially flatter than GM, in a manner similar to what was observed by Pinkel (1984), also in the upper ocean. This is another feature predicted by the model presented in section 7.

An excess of downward traveling energy (upward phase propagation) at near-inertial frequencies has been observed elsewhere in the upper ocean, but Pinkel (1984) reports a net upward energy flux (2.8 mW m^{-2}) integrated over frequencies f–$60f$ contributed mainly by frequencies higher than 0.2 cph (the near-inertial flux is ~0.5 mW m^{-2} downward). The LOTUS PCM records can resolve neither such small vertical wavenumbers nor such high frequencies, but they do indicate downward energy flux in all three bands (see Table 2) totaling 0.7 mW m^{-2} downward in P1G but less than a tenth this value in P1H. Despite the small values, the net flux is 10–20% of the magnitude of flux in the superinertial band and a somewhat smaller fraction in the semidiurnal tidal and supertidal frequency bands.

9. Discussion

The LOTUS PCM records indicate substantial variability in the upper ocean internal wave field, both in

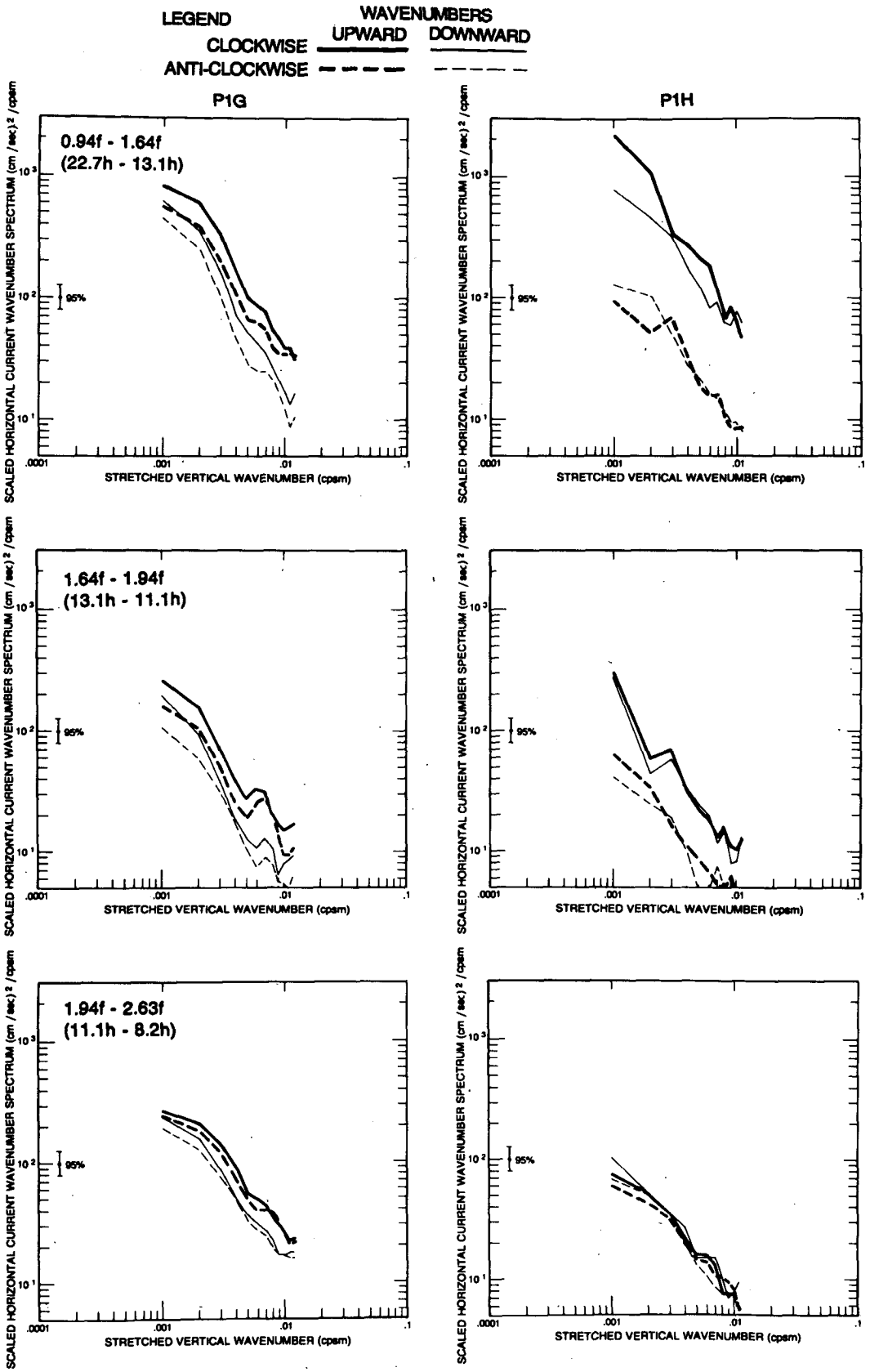

FIG. 10. Stretched vertical wavenumber spectra of clockwise and anticlockwise current in P1G and P1H for three different frequency bands (top: superinertial, middle: semidiurnal tidal, and bottom: supertidal).

TABLE 2. Estimates of internal wave vertical energy flux F in the stretched vertical wavenumber band 0.001–0.011 cpsm as expressed in 10^{-3} W m^{-2}.*

Frequency Band	Upward	Downward	Net (positive upward)
		P1G	
Superinertial 1.0f–1.64f (20.6–13.1 h)	0.362	0.568	−0.206
Semidiurnal tidal 1.64f–1.94f (13.1–11.1 h)	0.297	0.481	−0.184
Supertidal 1.94f–2.63f (11.1–8.2 h)	0.872	1.193	−0.321
		P1H	
Supertidal 1.04f–1.64f (20.6–13.1 h)	0.184	0.236	−0.052
Semidiurnal tidal 1.64f–1.94f (13.1–11.1 h)	0.234	0.274	−0.040
Supertidal 1.94f–2.63f (11.1–8.2 h)	0.340	0.320	0.038

* Flux F is estimated here as an integral

$$F = \int_\omega \int_m (S_+ + S_-)\left(-\frac{\omega}{m}\right)\left(\frac{\omega^2 - f^2}{\omega^2 + f^2}\right) d\omega dm$$

where $(S_+ + S_-)$ expresses the joint frequency wavenumber spectrum of anticlockwise and clockwise currents. F is independent of $N(z)$ and the reference value N_0 used for stretching and scaling.

depth and in time. Variation of the spectrum in depth through the seasonal pycnocline is a robust signal only near the inertial frequency, a feature which can be accounted for by a general property of response to traveling forcing. Temporal variations of the frequency–wavenumber shape, level, and partition between clockwise and anticlockwise components of the horizontal current spectrum are all observed. Internal wave energy is highly correlated with the rms speed of subinertial currents, suggesting that the upper ocean internal wave field is modulated locally. The models of sections 6 and 7 are attempts to explain depth and time variability, respectively.

Adaption of the Kundu and Thomson model to explain the specific inertial peak depth dependence observed in LOTUS would require observations of the spatial and temporal structure of many frontal passages. Random superposition of propagating wind systems can be expected to degrade any coherence of near-inertial currents with local winds, a result which is consistent with the lack of coherence reported by Briscoe and Weller (1984) in LOTUS. Yet broadband response to random forcing leaves a recognizable signature, nonetheless, in the depth dependence of the inertial peak. The magnitude of inertial peak height change and blue shift with depth predicted by the model forced by a single line source is consistent with what is observed (i.e., a factor of 5 or so change in peak height and a shift from f to 1.1f over 100 m depth).

Inertial peak blue shifts have been reported in deep measurements and explained as the result of internal waves propagating from lower latitudes to their latitudinal turning points (see Fu 1981). But the blue shifts reported are only about half what is observed near the bottom of the seasonal pycnocline in LOTUS. A wind-forced response model predicts blue shift of the observed magnitude as the result of dispersion in internal wave wakes, a local, rather than global, mechanism.

Temporal variability of the internal wave field and relationships to subinertial time scale flows have been observed by others. Frankignoul (1974, 1976) found that internal waves of moderate frequencies tend to be aligned across the direction of mesoscale eddy flows. Frankignoul and Joyce (1979) and Ruddick and Joyce (1979) searched for evidence that internal waves interact with vertical shear of mesoscale eddies with little success. Rather, the latter authors found a correlation of internal wave vertical flux of horizontal momentum with mesoscale current speed. Brown and Owens (1981) found at most a weak correspondence between internal wave horizontal stress with horizontal shear. Recently, Kunze and Sanford (1984) and Kunze (1986) have presented evidence that near-inertial internal wave energy is enhanced within regions of relative vorticity of opposite sign to planetary vorticity in upper ocean fronts and warm-core rings. Though the observational base is scant, the evidence points to horizontal structure in subinertial time scale flows being at least as important in causing temporal variability in internal wave statistics as vertical shear of these motions.

The influence of geostrophic currents on internal wave propagation has been treated by a number of authors. Ivanov and Morozov (1974) consider an idealized barotropic current jet with piecewise-uniform horizontal shear and solve numerically for internal wave rays and amplitudes for a few specific frequencies and incident wavenumbers. Since the wave scales chosen in these simulations were short compared to the scales of the gross structure of the current specified, their results are very similar to the predictions of ray theory given here in section 7. Kunze's (1985) calculations focus on near-inertial waves, for the vorticity of the mean flow affects the propagation of these waves. In the ray traces he calculates, three effects tend to compete: modulation of the effective inertial frequency (by the vorticity of the mean flow) and conservation of wave action flux due to vertical and horizontal structure of the flow. In these latter two effects, the scale of the shear leading to changes in current speed is unimportant. Rather it is the Doppler shift itself that controls ray paths and energy density. Although the ray paths calculated by Kunze exhibit some of the characteristics predicted by the model considered in section 7, they are masked by characteristics due to

vertical critical layers and vorticity-trapping because the flows considered are fully baroclinic and have strong horizontal shear.

In contrast to the Kunze ray traces, the calculations made in section 7 depend solely on the magnitude of the current U (independent of the horizontal structure of the current) as long as relative vorticity is weak compared to planetary vorticity and (horizontal) critical layer and turning point effects can be neglected. Temperature sections in the LOTUS region (Trask and Briscoe 1983; Montgomery et al. 1984) indicate that mesoscale eddy scales are O(100 km) giving a relative vorticity scale of $O(10^{-2}f)$ so that vorticity trapping is unlikely to be important. The observed correlation between internal wave energy and subinertial speed (rather than horizontal shear) indicates the vorticity trapping mechanism is less important than wave action conservation for this region. Neglect of vertical shear effects is justifiable particularly at low internal wave frequencies (e.g., $f \leqslant \omega \leqslant 2.63f$, the range resolvable in the PCM observations) since ray paths are only gently inclined, hence horizontal variations in current are likely to modulate waves before vertical variations.

The modulations of the low-frequency portion of the internal wave spectrum due to moderate currents predicted by the model of section 7 are similar in magnitude and form to what is observed in the LOTUS PCM records. Higher current results in a less energetic inertial peak, a more energetic superinertial band, a decrease in rotary polarization, and a more energetic and flatter wavenumber spectrum at moderate (e.g., supertidal) frequencies. These are the principal differences in the observations between a low-current (P1H) and high current (P1G) record. Given the GM spectrum as a representative basic state for the internal wave spectrum in a quiet ocean (i.e., subinertial currents of a few centimeters per second or less), the predicted spectrum from Doppler shifting by barotropic flows is remarkably similar in shape and level to what is observed.

As mentioned in the Introduction, the models presented here have not been tested against observations in the sense that they have been used to explain some fraction of the observed variance. Rather, the models have been used to mimic identifiable features in the observed spectra which, by their persistence, are presumed to be insensitive to forcing or environmental conditions. For both models, the predicted signals are of the same sense and magnitude as what was observed. More sophisticated tests of these models will be possible when more complete descriptions of forcing, environmental conditions, and internal wave variability are obtained concurrently.

Acknowledgments. I am indebted to the engineers and technicians at the C. S. Draper Laboratory for their incalculably valuable assistance in carrying out the PCM field work. Particular thanks in this regard are due J. Dahlen, J. Shillingford, and R. Reid. I thank Drs M. Briscoe and R. Weller for organizing and helping us participate in LOTUS and generously allowing us access to their data, and the officers and crew of R/V *Oceanus* and R/V *Endeavor* and personnel of the Woods Hole Oceanographic Institution Moored Array Project for their able assistance at sea. I benefited from valuable scientific discussions with Drs R. Weller, R. Pinkel, and L. Talley during the course of the work. I thank S. Johnson and C. King for their loyal, able assistance in carrying out computations and S. Fagerberg for help in preparing the manuscript. Much of the analysis was carried out during a pleasant sabbatical visit to the Marine Physical Laboratory of the Scripps Institution of Oceanography. This work was supported by the Office of Naval Research under Contract N00014-80-C-0273 to the Massachusetts Institute of Technology.

APPENDIX

Evaluating the GM Spectrum

The Garrett–Munk spectrum is given by Munk (1981) as

$$E(\omega, j) = \frac{2}{\pi}\frac{f}{\omega}(\omega^2 - f^2)^{-1/2}\frac{(j^2 + j_*^2)^{-1}}{\sum_1^\infty (j^2 + j_*^2)^{-1}}(6.3 \times 10^{-5}) \tag{A1}$$

where internal wave energy density is expressed as a function of frequency ω and vertical mode number j where f is the inertial frequency and $j_* = 3$ is the transition mode number separating flatter from steeper vertical wavenumber dependence. The energy per unit mass per unit frequency bandwidth per vertical mode in horizontal currents is

$$b^2 N_0 N(z)\frac{1}{2}(1 \pm f/\omega)^2 E(\omega, j)$$

where the plus and minus signs are for the clockwise and anticlockwise components, respectively. In addition, $b = 1.3$ km and $N_0 = 3$ cph are scale factors and $N(z)$ is the local buoyancy frequency. If $\psi_j(z)$ are the vertical structure functions of horizontal current for baroclinic mode j calculated for a given $N(z)$ profile [assuming $\omega \ll N(z)$], then the spectra of clockwise and anticlockwise current S_- and S_+ are

$$S_\mp = (\omega, j) = \frac{1}{2} b^2 N_0 \bar{N}(1 \pm f/\omega)^2 E(\omega, j)\psi_j(z) \tag{A2}$$

where $\bar{N}$ is the depth averaged $N(z)$ and the ψ_j are normalized according to $\int_{-D}^0 \psi_j \psi_k dz = D\delta_{jk}$ where D is the ocean depth. To calculate frequency spectra (as in the dashed curves of Fig. 2), S_- and S_+ were summed over $j = 1$ to 30 instead of the infinite sum in (A1) and

adjusted downward to agree with the observations by dividing by 3. For the LOTUS region, $\bar{N} = 0.9435$ cph so the total variance $2b^2N_0\bar{N}\pi^{-1}6.3 \times 10^{-5} = 5.844$ cm^2/s^2 (prior to adjustment for comparison).

To calculate the Doppler-shifted spectra S_-, S_+ in (11) we take

$$E = b^2N_0NE(\omega, j)$$

in Eq. (9) where $N = 1$ cph and $\psi_j(z) = 1$ is chosen to represent implicitly a typical near-surface mixture of modes. Doppler shifts are calculated using $m_j = j\pi/D$, the vertical wavenumber appropriate to a constant N ocean.

REFERENCES

Bendat, J. S., and A. G. Piersol, 1971: *Random Data: Analysis and Measurement Procedures.* Wiley-Interscience, 407 pp.

Briscoe, M. G., and R. A. Weller, 1984: Preliminary results from the Long-Term Upper-Ocean Study (LOTUS). *Dyn. Atmos. Oceans,* **8,** 243–265.

Brown, E. D., and W. B. Owens, 1981: Observations of the horizontal interactions between the internal wave field and the mesoscale flow. *J. Phys. Oceanogr.,* **11,** 1474–1480.

Eriksen, C. C., 1987: Observations of the seasonal cycle of upper ocean structure and the roles of advection and diapycnal mixing. *J. Geophys. Res.,* **92,** 5354–5368.

——, J. M. Dahlen and J. T. Shillingford, 1982: An upper ocean moored current and density profiler applied to winter conditions near Bermuda. *J. Geophys. Res.,* **87,** 7879–7902.

Frankignoul, C., 1974: Observed anisotropy of spectral characteristics of internal waves induced by low-frequency currents. *J. Phys. Oceanogr.,* **4,** 625–634.

——, 1976: Observed interaction between oceanic internal waves and mesoscale eddies. *Deep-Sea Res.,* **23,** 805–820.

——, and T. M. Joyce, 1979: On the internal wave variability during the internal wave experiment (IWEX). *J. Geophys. Res.,* **84,** 769–776.

Fu, L.-L., 1981: Observations and models of inertial waves in the deep ocean. *Rev. Geophys. Space Phys.,* **19,** 141–170.

Ivanov, Yu.A., and Ye.G. Morozov, 1974: Deformation of internal gravity waves by a stream with horizontal velocity shear. *Okeanologie,* **14,** 376–380 (English translation).

Kundu, P. K., 1986: A two-dimensional model of inertial oscillations generated by a propagating wind field. *J. Phys. Oceanogr.,* **16,** 1399–1411.

——, and R. E. Thomson, 1985: Inertial oscillations due to a moving front. *J. Phys. Oceanogr.,* **15,** 1076–1084.

Kunze, E., 1985: Near-inertial wave propagation in geostrophic shear. *J. Phys. Oceanogr.,* **15,** 544–565.

——, 1986: The mean and near-inertial velocity fields in a warm-core ring. *J. Phys. Oceanogr.,* **14,** 566–581.

——, and T. B. Sanford, 1984: Observations of near-inertial waves in a front. *J. Phys. Oceanogr.,* **14,** 566–581.

Levine, M. D., 1983: Internal waves in the ocean: A review. *Rev. Geophys. Space Phys.,* **21,** 1206–1216.

Lighthill, J., 1978: Waves in Fluids. Cambridge University Press, 504 pp.

Montgomery, E. T., N. J. Pennington and M. G. Briscoe, 1984: The Long-Term Upper-Ocean Study (LOTUS) cruise summary and hydrographic data report Oceanus 141, October 1983, and Oceanus 145, January 1984. Woods Hole Oceanographic Institution Tech. Rep. WHOI-84-26.

Munk, W., 1981: Internal waves and small scale processes. *Evolution of Physical Oceanography.* B. A. Warren and C. Wunsch, Eds., MIT Press, 264–291.

Olbers, D. J., 1981: The propagation of internal waves in a geostrophic current. *J. Phys. Oceanogr.,* **11,** 1224–1233.

Pinkel, R., 1984: Doppler sonar observations of internal waves: The wavenumber–frequency spectrum. *J. Phys. Oceanogr.,* **14,** 1249–1270.

Ruddick, B. R., and T. M. Joyce, 1979: Observations of interaction between the internal wavefield and low-frequency flows in the North Atlantic. *J. Phys. Oceanogr.,* **9,** 498–517.

Trask, R. P., and M. G. Briscoe, 1983: The Long-Term Upper-Ocean Study (LOTUS) cruise summary and hydrographic data report *Endeavor* 97, April 1983. Woods Hole Oceanographic Institution Tech. Rep., WHOI-83-33.